

## Article

# Partial Replacement of Dimethylformamide with Less Toxic Solvents in the Fabrication Process of Mixed-Halide Perovskite Films

Viorica Stancu <sup>\*</sup>, Andrei Gabriel Tomulescu, Lucia Nicoleta Leonat, Liliana Marinela Balescu , Aurelian Catalin Galca , Vasilica Toma, Cristina Besleaga, Sarah Derbali and Ioana Pintilie 

National Institute of Materials Physics, Atomistilor 405A, 077125 Magurele, Romania

\* Correspondence: stancu@infim.ro

**Abstract:** The technology of perovskite solar cells (PSC) is getting close to breaching the consumer market. Yet, one of the current challenges is to reduce the toxicity during their fabrication by reducing the use of the toxic solvents involved in the perovskite fabrication process. A good solubilization of lead halides used in hybrid perovskite preparation is required, and it is only possible with polar solvents. A mixture of dimethylformamide (DMF) and dimethyl sulfoxide (DMSO) is the most popular solvent combination for a perovskite precursor solution. DMF is necessary to ensure a good dissolution of lead iodide, but it is also the most toxic solvent. In this paper, we study the replacement of the dimethylformamide with presumably less toxic alternatives, such as N-methyl-2-Pyrrolidone (NMP) and ethyl acetate (EA), for the preparation of the  $K_{0.1}FA_{0.7}MA_{0.2}PbI_{2.8}Cl_{0.2}$  (KFAMA) hybrid perovskite. The perovskite thin films were investigated by various characterization techniques: X-ray diffraction, atomic force microscopy, scanning electron microscopy, and UV–vis spectroscopy, while the photovoltaic parameters were determined by measuring the IV curves of the corresponding solar cells. The present study shows that by keeping the same deposition parameters as when only DMF solvent is used, the partial solvent substitution with NMP and EA gives promising results for reducing the toxicity of the fabrication process of KFAMA-based PSCs. Thus, with no specific optimization of the deposition process, and for the maximum possible partial substitution of DMF with NMP and EA solvents, the loss in the power conversion efficiency (PCE) value is only 35% and 18%, respectively, associated with the more structural defects promoted by NMP and EA.

**Keywords:** DMF partial substitution; EA; NMP; perovskite solar cells



**Citation:** Stancu, V.; Tomulescu, A.G.; Leonat, L.N.; Balescu, L.M.; Galca, A.C.; Toma, V.; Besleaga, C.; Derbali, S.; Pintilie, I. Partial Replacement of Dimethylformamide with Less Toxic Solvents in the Fabrication Process of Mixed-Halide Perovskite Films.

*Coatings* **2023**, *13*, 378. <https://doi.org/10.3390/coatings13020378>

Academic Editor: Feng Wang

Received: 9 January 2023

Revised: 31 January 2023

Accepted: 3 February 2023

Published: 7 February 2023



**Copyright:** © 2023 by the authors. Licensee MDPI, Basel, Switzerland. This article is an open access article distributed under the terms and conditions of the Creative Commons Attribution (CC BY) license (<https://creativecommons.org/licenses/by/4.0/>).

## 1. Introduction

Finding new materials to convert the sun's energy into electricity is a challenge for all of mankind. This need is even more serious nowadays, due to the growing population coupled with the problem of climate change caused by industrialization. In the photovoltaic field, perovskite solar cells (PSC) have attracted attention due to their high power conversion efficiency (PCE) [1]. Most studies focus on perovskites with the general formula  $CH_3NH_3PbX_3$  ( $X = Cl, Br^-$  and  $I^-$ ), which present excellent properties, such as good light-absorption, high carrier mobility, and, not least, facile processability [2–6]. The challenges impeding the transition to industry are related to their stability in time and reproducibility of performance. Additionally, the most important environmental problems arise from the use of toxic elements/solvents [7–9] during the preparation of the precursor solutions.

Solvent engineering is a necessary step in the development of thin film fabrication for solar cells. The solvent role is very important for the coordination with the lead salt in order to form a lead salt–solvent complex. Dimethylformamide (DMF) is the most common solvent used for the preparation of organic–inorganic halide perovskite precursor solutions. Using polar aprotic solvents such as dimethyl sulfoxide (DMSO), gamma-butyrolactone

(GBL), or *N*-methyl-2-pyrrolidone (NMP), in addition to DMF, greatly improves the morphology of the perovskite film obtained in a single-step deposition [8,10]. The polarity of the aprotic solvent determines the degree of binding to  $\text{Pb}^{2+}$  and thus the stability of the complex. The choice of aprotic solvent in the precursor solution is very important for preparing good-quality films. Usually, the perovskite precursor solution is prepared using a DMF and DMSO mixture, where the DMF acts as the solvent for its excellent lead iodide dissolution, and DMSO acts as the ligand because of its strong coordination capabilities to  $\text{Pb}^{2+}$  [11,12]. However, of all the solvents used for halide perovskites, DMF possesses the highest toxicity, according to the classification made by the European Chemicals Agency (ECHA), (<https://echa.europa.eu/information-on-chemicals> (19 December 2022)). The problem of the solvent types and the ratio of their mixtures was investigated by Cai et al. [13] for  $\text{MAPbI}_3$  perovskite. They used a mixture of DMF: DMSO as the solvent for the precursor solution preparation, where the DMSO has a double role, acting both as a solvent and a coordinating agent, while the DMF acts as the main solvent to dissolve the Pb salt. Recently, only a few “green” solvents have been studied as additives or antisolvents [14], or as a replacement for DMF, although the PCE of the corresponding devices is still lower than that of the DMF-based cells [15]. Solar cell fabrication involves an antisolvent treatment to initiate the crystallization of the perovskite film and facilitate the removal of the host solvent. Chlorobenzene (CB) is usually selected as an antagonist solvent, or antisolvent, owing to its insolubility in the mixed perovskite precursor solution, miscibility with DMF and DMSO, and it helps stabilize the formation of a crystalline perovskite phase [16].

It is well known that the solvent characteristics have a big influence on the hybrid perovskite formation [12,17–19]. To be precise, the polarity index of the solvents affects the coordination process with the lead halide salts, which further influences the formation of the intermediate compounds and lead–solvent complexes, such as  $\text{MAI}\cdot\text{PbI}_2\cdot\text{DMSO}$  adduct [17]. The presence of these chemical species determines the morphology of the active layer and their defect density [20]. The use of DMF as the solvent leads to a random orientation of the perovskite crystals, while the mixture of DMF and DMSO induces the formation of perovskite crystals perpendicular to the substrate [21]. When solely DMF is used, its relatively rapid evaporation induces fast nucleation and crystallization of small grains. When DMF is mixed with DMSO, it slows down the nucleation rate, so the crystals grow perpendicularly to the substrate and present a bigger crystalline size [22].

Another aspect concerning the fabrication of perovskite films with good morpho-structural properties is the choice of the antisolvent. Konstantakou et. al. [23] studied the effect of the antisolvent on the device performance, and they concluded that this element has a huge influence on the efficiency (chlorobenzene generating the best performance), along with an optimum time for the addition of the antisolvent during the perovskite precursor solution dynamic spin-coating deposition [10].

In this article, we present a *mixed-solvent dilution strategy* to reduce the DMF quantity and maintain the high quality of the perovskite films. In the literature, EA has been used only as an antisolvent. In our study, EA is used as a solvent. The influence of the partial replacement of DMF in the DMF: DMSO mixture with NMP-*N*-methyl-2-pyrrolidone and EA—ethyl acetate in the  $K_{0.1}\text{FA}_{0.7}\text{MA}_{0.20}\text{PbI}_{2.8}\text{Cl}_{0.2}$  (KFAMA) perovskite was thoroughly investigated in order to determine the structural, optical, and morphological properties of the perovskite films, and how these properties influence the photovoltaic performances of the fabricated solar cells.

## 2. Materials and Methods

The raw materials (precursors and solvents) were used as purchased, without further purification: lead iodide ( $\text{PbI}_2$ , 99%), lead chloride ( $\text{PbCl}_2$ , 99.99%), *N,N* Dimethylformamide (DMF), dimethyl sulfoxide (DMSO, 99%), 1*N*-methyl-2-Pyrrolidone (NMP, 99.5%) and ethyl acetate (EA, 99%), chlorobenzene (CB), acetone, isopropanol (IPA, 98.5%), acetonitrile (99.8%) and anhydrous ethanol (96%), 4-*tert*-butylpyridine (tBP, 99.99%), lithium bis(trifluoromethanesulfonyl)imide (LiTFSI, 99.99%), and titanium diisopropoxide

bis(acetylacetonate) ( $\text{Ti}(\text{iProp})_2\text{AcAc}_2$ , 75% solution in 2-propanol) were purchased from Sigma Aldrich of Alfa Aesar (Ward Hill, MA, USA). Methylammonium iodide (MAI, 99%) and formamidinium iodide (FAI, 99.9%) were purchased from Greencell (Kraków, Poland), and potassium iodide (KI, 99.99%) was purchased from Merck (Darmstadt, Germany). The spiro-OMeTAD (99.99%) was purchased from Borun New Material Technology LTD (Ningbo, China), Ti-Nanoxide T/SP from Solaronix, and  $\text{SnO}_2$  from Alfa Aesar, respectively.

*Preparation of  $K_x\text{FA}_{0.80-x}\text{MA}_{0.20}\text{PbI}_{2.8}\text{Cl}_{0.2}$  ( $x = 0.10$ ) perovskite formulations:* To prepare the  $\text{K}_{0.1}\text{FA}_{0.7}\text{MA}_{0.20}\text{PbI}_{2.8}\text{Cl}_{0.2}$  solutions, MAI, FAI,  $\text{PbI}_2$ ,  $\text{PbCl}_2$ , and KI were dissolved in a solvent mixture of 8.2:1 DMF: DMSO (600 mg of DMF and 78 mg of DMSO). The DMF was substituted in a different quantity and with different solvents in order to see how the solar cells' efficiency was influenced. The sample notation, the solvents used, and their ratios are presented below in Table 1. CB was used as an antisolvent for all the samples.

**Table 1.** The solvent ratio used in the KFAMA precursor solution.

Notation	Solvents Used	Molar Ratio
DMF	DMF:DMSO	8.2:1
NMP	DMF:NMP:DMSO	4.1:4.1:1
EA	DMF:EA:DMSO	5.74:2.46:1

We performed preliminary experiments on the solubilization of Pb salts in the selected solvent mixtures, in variable ratios, to keep the molar concentration of the perovskite precursor solution at a constant value of 1.415 M. The percentages of EA and NMP used in this study were the maximum that allowed the solubilization of Pb salts. Above these values, the salts are no longer solubilized completely.

*Thin film fabrication:* The perovskite solutions were filtered through a 0.45  $\mu\text{m}$  PTFE syringe filter to remove undissolved particles, and 100  $\mu\text{L}$  of KFAMA solution was deposited by spin coating at 2000 rpm for 25 s. After 15 s from the start of the spin coating process, 100  $\mu\text{L}$  CB was dropped to assist the perovskite crystallization. The perovskite film formation was completed after annealing at 140  $^\circ\text{C}$  for 3 min on a hot plate. The entire process took place inside a nitrogen-filled MBraun professional glove box with  $\text{H}_2\text{O} < 0.1$  ppm and  $\text{O}_2 < 0.1$  ppm.

*Solar Cell Fabrication:* Pre-patterned fluorine tin oxide (FTO,  $16 \times 25 \times 1.1 \text{ mm}^3$ ) with a sheet resistance of 15  $\Omega$  per square was purchased from Xin Yan Technology LTD (Kowloon, Hong Kong). The FTO substrates were cleaned by sonication in a detergent solution, and then with distilled water, acetone, and IPA, each for 10 min by sequential sonication. Before the spin coating, the FTO-coated glass substrates were exposed to 0.7 mbar oxygen plasma for 10 min to remove the remaining organic contamination and dust from the surface. A compact  $\text{TiO}_2$  layer was deposited as the n-type layer by spray pyrolysis, using  $\text{Ti}(\text{iProp})_2\text{AcAc}_2$  in IPA (1:30 volumetric ratio) at 450  $^\circ\text{C}$ , followed by thermal treatment at 450  $^\circ\text{C}$  for 30 min. Then, mesoporous  $\text{TiO}_2$  was deposited, using a dispersion of  $\text{TiO}_2$  nanoparticles in ethyl alcohol (1:200 by weight) at 100  $^\circ\text{C}$ . The mesoporous structure was complete after sintering at 500  $^\circ\text{C}$  for 60 min. The deposition of the perovskite active layer was carried out as described above in the thin film fabrication section.

For the p-type layer, 80 mg of spiro-OMeTAD and 18  $\mu\text{L}$  of tBP were dissolved in 1 mL of CB and mixed with 28  $\mu\text{L}$  Li-TSFI salt solution (520 mg/1 mL acetonitrile). This mixture was spin-coated at 3000 rpm for 50 s, and the samples were left overnight in a  $\text{N}_2$  atmosphere to dry. Top gold (Au) electrodes ( $\sim 100 \text{ nm}$ ) were deposited by magnetron sputtering through a shadow mask to define the devices with active areas of 0.083  $\text{cm}^2$ .

The crystal structure was studied using a Bruker-AXS D8 Advance diffractometer employing a LynxEye 1D detector, a Cu-K $\alpha$  ( $\lambda = 0.1541 \text{ nm}$ ) radiation source (Karlsruhe, Germany), and a scintillation counter detector. The data were collected from 8 $^\circ$  to 40 $^\circ$  using a scan speed of 1 s per step and a step size of  $2\theta = 0.02^\circ$ . For the identification of the XRD phases present in the samples, the Powder Diffraction Files from the International Center for Diffraction Data (PDF-ICDD) were used. The morphology of the perovskite films was

investigated with a Gemini500 Scanning Electron Microscope from Zeiss (Jena, Germany) and an NT-MDTAura Ntegra Prima Atomic Force Microscopy system (AFM) (Amsterdam, The Netherlands) in noncontact mode. The optical measurements were inferred by using a V-VASE Woollam spectroscopic ellipsometer (Lincoln, NE, USA) equipped with a high-pressure Xe discharge lamp incorporated in an HS-190 monochromator in conventional spectroscopy mode.

*Current Density–Voltage Characteristics:* J–V curves were recorded at a low scanning rate of 20 mV/s under ambient conditions in the forward and reverse scan directions, starting from the open-circuit voltage to  $-0.1$  V to avoid unwanted poling, using a solar simulator with AM 1.5 G solar radiation, with an incident power of  $100 \text{ mW/cm}^2$  coupled with a Keithley source 2601.

The main parameters calculated from the J–V curves were the short-circuit current density,  $J_{sc}$ , the open-circuit voltage,  $V_{oc}$ , the fill factor, FF, and the series and shunt resistances  $R_s$ ,  $R_{sh}$ , respectively. The hysteresis factor,  $H_i$ , was calculated as described in reference [24] as the ratio between the area defined by the reverse (R) and forward (F) scans of one sample, and the sum of the areas under the forward and reverse curves in the range of 0 to  $V_{oc}$  value. In this case, the hysteresis formula is simplified due to the absence of an intersection between the two scan directions, becoming:

$$H_i = \frac{A_R - A_F}{A_R + A_F} \times 100, \quad (1)$$

where  $A_R$  and  $A_F$  represent the area under the reverse (R) and forward (F), respectively, between 0 and  $V_{oc}$ .

The power conversion efficiency (PCE) was calculated using the well-known formula of dividing the output power of the device (obtained from the measured J–V curves) by the input power of the solar simulator and the active area of the device ( $0.083 \text{ cm}^2$ , in this case).

### 3. Results and Discussion

The solar cells (PSCs) studied here have the following architecture: glass/FTO/TiO<sub>2</sub>c-m/K<sub>0.1</sub>FA<sub>0.7</sub>MA<sub>0.20</sub>PbI<sub>2.8</sub>Cl<sub>0.2</sub>/spiro-OMeTAD/Au. For the fabrication of ETL layers, we used a common laboratory method, spray deposition [25]. This method leads to a porous, reticulated structure with well-delimited and irregular cavities, with non-uniform thickness, and diameters in the range of 3–10  $\mu\text{m}$  (see Figure 1). At the bottom of the cavities, the mesoporous TiO<sub>2</sub> has a thickness of 150–200 nm, while, on the peaks, the mesoporous thickness can reach up to 500 nm. The compact TiO<sub>2</sub> film is uniformly deposited on the entire FTO surface and is approximately 100 nm thick. This specific structure allows the deposition of a thicker perovskite layer and increases the surface of the ETL–perovskite interface.

The AFM images of the perovskite layers reveal consistent films. The rugosity varies between the samples, with the DMF sample presenting an RMS of 69 nm. The partial substitution of the DMF solvent leads to an increase of the RMS to 110 nm for the EA samples, and to a small decrease, to 62 nm, in the case of the NMP.

For all the samples, the ETL layer (TiO<sub>2</sub>c-m) presents a relatively constant thickness in a range of 250–300 nm. The perovskite average thickness was also measured and ranges from 983 nm for the DMF samples to 1493 nm in the case of the EA (see Figure 1). Perovskite films using NMP have an average thickness of 870 nm. The differences are due to the nature of the solvent [26], different polarity (EA), and/or density (NMP) of the solvents, which influence how the precursor solution wets the substrate, along with its crystallization, and the coordination of the precursor salts with the solvent. The perovskite layer observed in the cross-section view presents a compact and dense structure, which is the key to good performance and stable perovskite solar cells. One of the key factors leading to obtaining a compact active film is the CB antisolvent [27]. No pinholes or cracks on the surface of the layer were observed, even in the case of high-rugosity films.

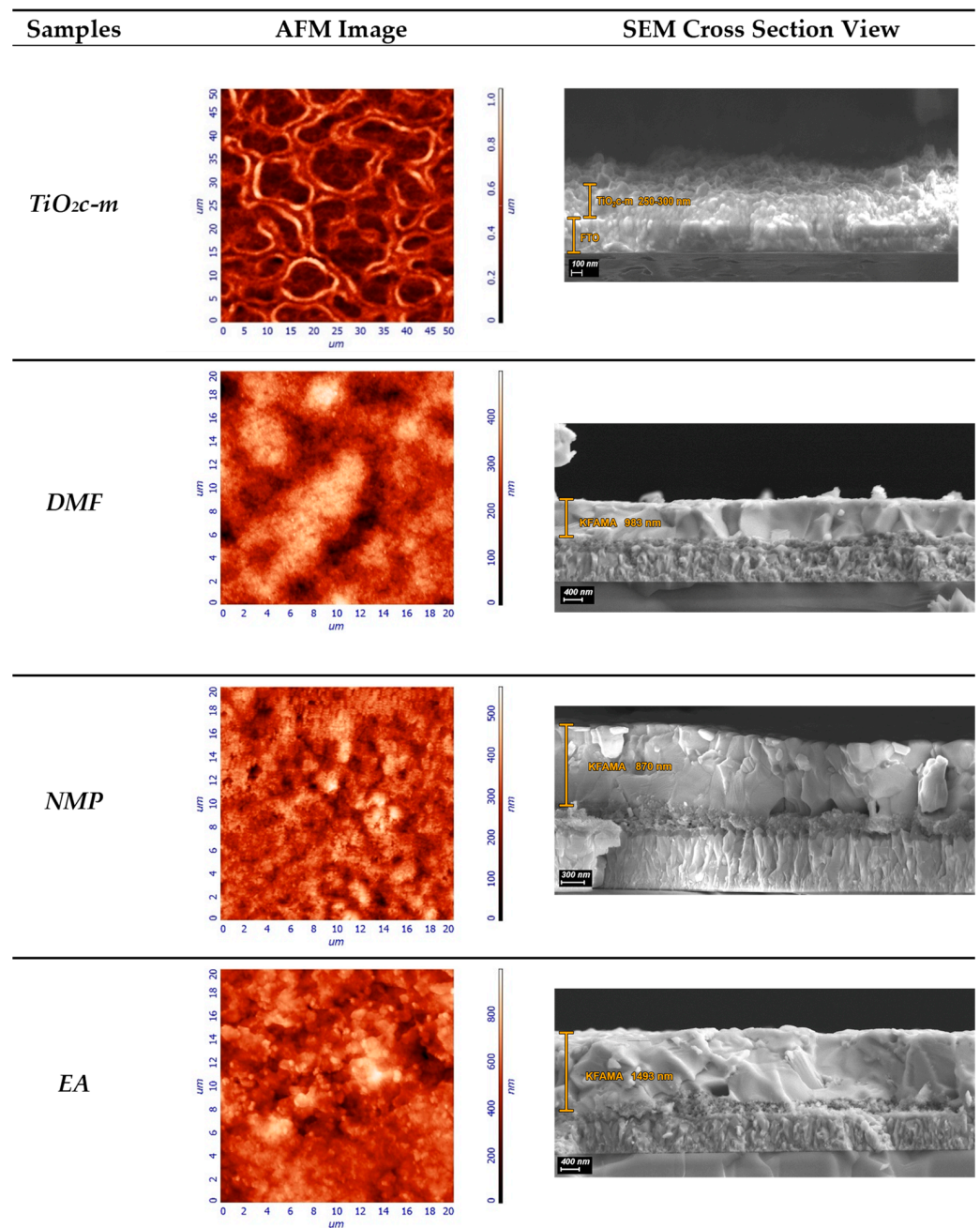


**Figure 1.** Surface AFM and cross-section SEM images for perovskite and ETL layers.

The XRD diffractograms of the fresh films are shown in Figure 2. All the analyzed samples show the same diffraction peaks at  $2\theta$ :  $13.98^\circ$ ,  $19.81^\circ$ ,  $24.34^\circ$ ,  $26.57^\circ$ ,  $28.19^\circ$ ,  $31.58^\circ$ , and  $34.73^\circ$ , corresponding to (101), (110), (021), (013), (202), (211), and (122) lattice planes of the  $\alpha$ -phase perovskite, according to ICDD 01-084-2961. In the presence of EA, the peak at  $2\theta = 11.45^\circ$  is correlated with the  $\delta$ -phase, which is the yellow non-perovskite undesirable phase [ICDD 01-084-296]. For all three samples analyzed here, the peak at  $2\theta = 12.64^\circ$  is correlated with the  $\text{PbI}_2$  presence [ICDD 00-007-0235]. Crystalline lead iodide ( $\text{PbI}_2$ ) is oriented as a secondary phase along the (00c) direction showing peaks at  $12.67^\circ$  (001),  $25.51^\circ$  (002), and  $38.66^\circ$  (003), with the highest peak at  $12.67^\circ$  (001). Analyzing carefully the XRD spectra, a very small peak appears at  $38^\circ$  for the perovskite with DMF and EA. There is no other perovskite phase or raw material with a diffraction line at this angle. Considering that only  $>99\%$  purity precursor powders were used, the diffraction signals attributed to the  $\text{PbI}_2$  and  $\delta$ -FAPbI<sub>3</sub> phases cannot be generated by impurities, since the

amount is below the detection limit of the diffractometer. For the secondary  $\delta$ -FAPbI<sub>3</sub> phase, the most intense signal is detected and located at 11.79° (100). The corresponding peaks (200 and 300) located at 23.71° and 35.89°, respectively, are not detected due to the small amount of secondary phase and the reduced intensity of the diffraction lines at those angles (according to ICDD 01-084-2966).

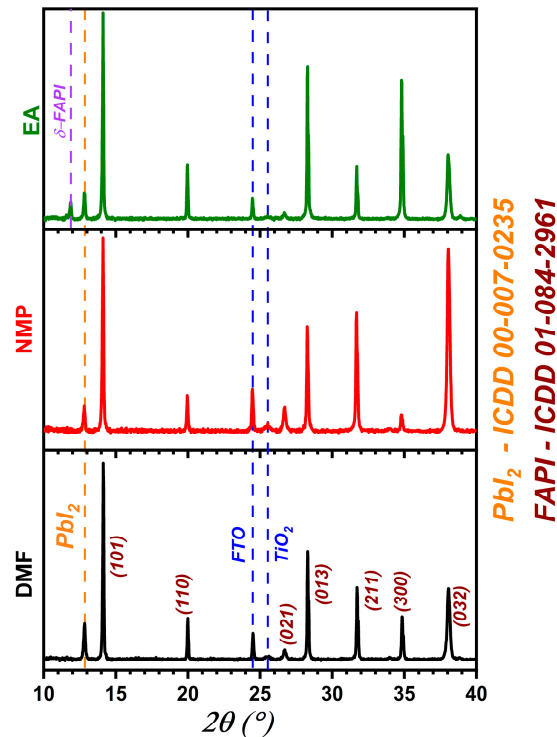


Figure 2. X-ray diffraction of the perovskite films prepared with different solvent mixtures.

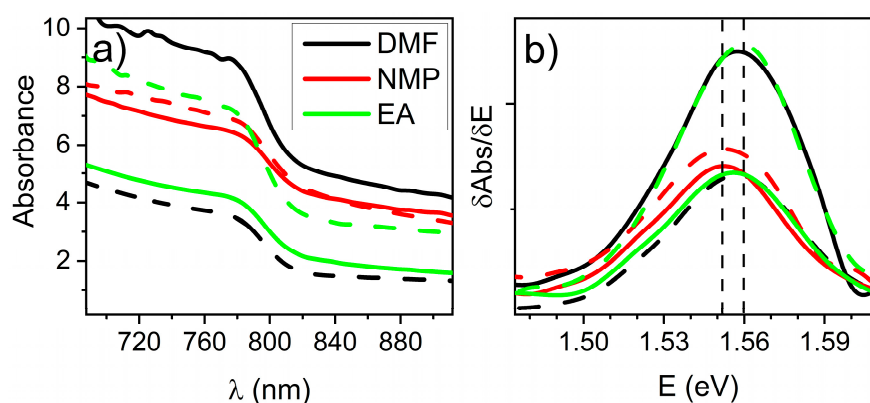
The perovskite crystallite size was estimated by the Scherrer equation [28], using the full width at half maximum of the (101) perovskite peak (Table 2). Perovskite films have similar crystallite size ranges in the case of NMP or EA mixtures, around 100 nm, comparable to the literature reports [29].

Table 2. Crystallite size and corresponding band gap values of fresh samples.

Notation	Perovskite Thickness (nm)	Crystallite Size (nm)	RMS (nm)	E <sub>g</sub> (eV)
DMF	983	121	69	1.56
NMP	870	96	62	1.55
EA	1493	118	110	1.55

Each absorbance spectrum was derived with respect to the photon energy to determine the inflection point, which corresponds to the band gap. The method mentioned by Shen [30] is a user-independent method, and it can be verified in comparison with the photoluminescence measurements [30–33]. The derivative method was recently used to determine the band gap of organic perovskite [34] and chalcogenide films [35].

The optical measurements (Figure 3). were performed with a step of 0.01 eV. The probed samples were both fresh perovskite films (organic perovskite deposited on TiO<sub>2mc</sub>/FTO/Glass substrates) and final devices (measurements done between the gold contacts). For all the samples, the band gaps are between 1.55 and 1.56 eV, the differences being within the step size of the measurements.



**Figure 3.** (a) Typical absorbance spectra of the perovskite structures obtained using different solvents on fresh samples (line) and devices (dash line). (b) Graphical representation of the method used to assess the samples' band gap, on fresh samples (line) and devices (dash line). Different areas of each sample have been measured. Note: different positions of each sample have been inspected; the incident light spot has a diameter of approximately 2 mm.

The effect of solvents on the solar cell efficiency values can be observed by analyzing the photovoltaic properties obtained by current–voltage ( $J$ – $V$ ) characteristics, reverse and forward scan, performed on the solar cells under simulated one sun illumination (AM 1.5 G). The average photovoltaic values obtained for each composition are presented in Table 3.

**Table 3.** Photovoltaic characteristics represented as average values of 16 solar cells for each composition.

Samples	$V_{oc}$ (V)	$J_{sc}$ (mA/cm <sup>2</sup> )	FF (%)	$R_s$ (Ω cm <sup>2</sup> )	$R_{sh}$ (Ω cm <sup>2</sup> )	$H_i$ (%)	PCE (%)		
							F	R	Avg.
DMF	0.992	21.3	48	15	574	13.4	7.95	12.35	10.15
NMP	0.809	17.1	48	11	378	2.9	6.40	6.82	6.61
EA	0.966	16.1	53	13	263	18.8	6.21	10.47	8.34

An open circuit voltage ( $V_{oc}$ ) close to 1 V was measured only for the samples with DMF. When using EA, a small drop of the average  $V_{oc}$  occurs, to a value of 0.966 V. The partial substitution of the DMF with NMP has a very detrimental effect on the  $V_{oc}$  of the solar cells, causing a loss of 18% compared with the DMF-based devices, leading to a final value of only 0.8 V. Short circuit current ( $J_{sc}$ ) does not present the same behavior. Our experiment shows that the devices with classical DMF: DMSO mixture present a good  $J_{sc}$ , of over 21 mA/cm<sup>2</sup>, in contrast to the samples with partial solvent substitution that experience a drop between 20 to 25%. Both the FF and the  $R_s$  have close values irrespective of the solvents used, while more significant variation is observed for the  $R_{sh}$ . From the  $J$ – $V$  curves corresponding to the champion devices featured in Figure 4, three distinct behaviors are noticeable, depending on the type of sample. We also evaluate the hysteresis [24] of KFAMA current-voltage curves illustrated in Figure 4. The  $H_i$  factor is to some extent linked to the quantity of defects, which further influences the degradation rate of the solar cells. The “classic” DMF cell presents a typical  $J$ – $V$  characteristic with a visible hysteresis. The average  $H_i$  factor in this case is 13.4% (see Table 3). While the appearance of hysteresis in  $J$ – $V$  curves, seen in all our cases, is typical for PSCs, its magnitude and shape, accounted in  $H_i$  factor, is related to ion migration, ion-induced defects, and charge accumulation at the interfaces [36,37]. The higher the magnitude of such microscopic processes, the larger the  $H_i$  factor. Different from the shapes of NMP and DMF curves, the shape of EA curve presents a large “bump” on the reverse scan of  $J$ – $V$  characteristics and a counter one in the forward bias scan. These “bumps” indicate different charge collection rates in the reverse and forward directions of the  $J$ – $V$  curves, enhanced in reverse and diminished in forward scan due to a favorable or

unfavorable polarization of the sample caused by ion migration, respectively [38]. This leads to a very high average value of the  $H_i$  factor, of over 18%, as a result of applying the Equation (1). All of these cause a severe drop in the average PCE when the DMF solvent is partially substituted with EA. The FF value is artificially increased by the “bump” in the reverse scan, overestimating thus the real value. In the case of NMP, the drop in efficiency is even worse, with the  $J_{sc}$  loss being accompanied by the large drop of the  $V_{oc}$  to 0.8 V.

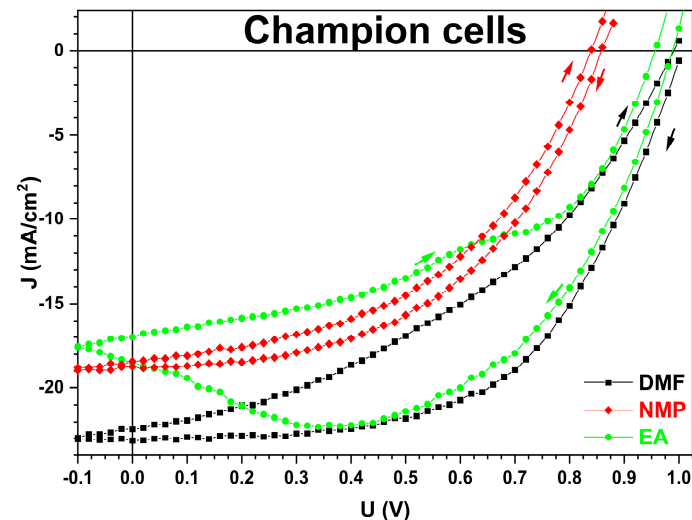


**Figure 4.** Photovoltaic characteristics for the champion PSCs obtained with different solvents. The arrows point towards the direction of the measurements (starting from the  $V_{oc}$  to  $J_{sc}$  and backwards).

The source of this behavior is complex. The morpho-structural improvement of the film quality is the key to obtaining efficient solar cells. The presence of hysteresis is a widely debated topic. The ion migration, charge recombination, charge carrier transport, or measurement procedure are identified as the main culprits in the hysteresis [39–41]. In this case, we associate the differences depicted in our study with the quality of the film [22,42], which is confirmed by the XRD, SEM, and AFM analyses. The EA sample presented an additional secondary  $\delta$ -phase, as seen in the X-ray diffraction, alongside the typical lead iodide, indicating a poorer perovskite layer quality, and an increased number of bulk defects, which is shown by the AFM images, whereas the EA presents a surface almost twice as rough in comparison with the other two. This is readily confirmed by the J–V measurements, where an unexpected “bump” appears only for the EA sample. The  $J_{sc}$  loss in the case of the NMP samples is partially due to a thinner perovskite film, with a thickness decrease of over 10%. A thinner layer of KFAMA means fewer photogenerated charge carriers, so lower  $J_{sc}$ . For the samples with EA, although the layer is thicker and more carriers are generated, the layer contains more defects, as highlighted by the shape of the J–V curve and confirmed by the AFM images, leading to more recombination and traps, ultimately generating considerable current losses. The J–V curve and the small  $H_i$  indicate that the interface recombination is dominant. It is known that NMP forms more stable adducts with lead salts than DMSO [43]. Also, Zhu et al. demonstrated perovskite passivation using a compound with maleimide functional groups, which are similar to NMP, in order to control the nucleation and crystallization process [44]. Considering that NMP has a high boiling temperature (of 202 °C), and that only a 3 min thermal treatment was applied during the film deposition, it is possible that a part of the NMP solvent was not completely eliminated from the film. Contrary to using a long molecule for passivation, NMP renders, at the interface, but does not bind multiple perovskite molecules, as it only possesses one functional group and has a detrimental effect on the photovoltaic performance, thus causing losses in  $J_{sc}$  and  $V_{oc}$ .

#### 4. Conclusions

We summarize that the choice of solvent is very important in the process of obtaining solar cells with the best possible performance. Both NMP and EA prove to be viable candidates for reducing the toxicity of perovskite precursor solutions. Notably, there are limitations to the substitution of DMF, which cannot be completely replaced for perovskites containing lead halides. Amongst all the solvents studied here, EA is the least harmful and can be a viable candidate for DMF substitution, due to its ability to dissolve the Pb salts properly.

However, it seems that the quality of the perovskite films is lower with this solvent mixture, DMF:EA:DMSO, which induces the appearance of a greater number of defects; therefore, the corresponding solar cells showed a lower average efficiency of 8.34% for the EA samples and of 6.61% for the NMP, than in the classical case of DMF:DMSO cells, which present a PCE of 10.15%. The mechanisms of this phenomenon for the KFAMA perovskite are not yet known and require additional in-depth studies.

**Author Contributions:** Methodology, V.S., L.N.L. and I.P.; software, A.G.T., A.C.G. and V.S.; validation, L.N.L., V.S., A.G.T., S.D. and C.B.; formal analysis, A.G.T., L.N.L., L.M.B. and C.B.; investigation, V.S., L.N.L., L.M.B., A.C.G. and V.T.; resources, I.P.; data curation, A.G.T. and V.S.; writing—original draft, V.S.; writing—review & editing, A.G.T., L.N.L. and I.P.; visualization, V.S., A.G.T., L.N.L. and L.M.B.; supervision, I.P.; project administration, I.P.; funding acquisition, I.P. All authors have read and agreed to the published version of the manuscript.

**Funding:** The research leading to these results received funding from the EEA Grants 2014–2021, under Project contract No. 36/2021, project code: EEA-RO-NO-2018-0106 and the Core Program 2023–2027, contract PN-23-08, from Romanian Ministry of Research and Innovation.

**Institutional Review Board Statement:** Not applicable.

**Informed Consent Statement:** Not applicable.

**Data Availability Statement:** The data are contained within the article.

**Acknowledgments:** The authors also thank Mihaela Florea for the fruitful discussions.

**Conflicts of Interest:** The authors declare no conflict of interest.

#### References

1. National Renewable Energy Laboratory. Best Research-Cell Efficiency Chart (National Renewable Energy Laboratory, 2021). Available online: <https://www.nrel.gov/pv/assets/images/efficiency-chart.png> (accessed on 19 December 2022).
2. Im, J.-H.; Lee, C.-R.; Lee, J.-W.; Park, S.-W.; Park, N.-G. 6.5% efficient perovskite quantum-dot-sensitized solar cell. *Nanoscale* **2011**, *3*, 4088–4093. [CrossRef]
3. Sum, T.C.; Mathews, N. Advancements in perovskite solar cells: Photophysics behind the photovoltaics. *Energy Environ. Sci.* **2014**, *7*, 2518–2534. [CrossRef]
4. Dong, Q.; Fang, Y.; Shao, Y.; Mulligan, P.; Qiu, J.; Cao, L.; Huang, J. Electron-hole diffusion lengths >175  $\mu\text{m}$  in solution-grown  $\text{CH}_3\text{NH}_3\text{PbI}_3$  single crystals. *Science* **2015**, *347*, 967–970. [CrossRef]
5. Zhang, Z.; Wang, M.; Ren, L.; Jin, K. Tunability of Band Gap and Photoluminescence in  $\text{CH}_3\text{NH}_3\text{PbI}_3$  Films by Anodized Aluminum Oxide Templates. *Sci. Rep.* **2017**, *7*, 1918. [CrossRef]
6. Chang, J.; Chen, H.; Wang, G.; Wang, B.; Chen, X.; Yuan, H. Electronic and optical properties of perovskite compounds  $\text{MA}_{1-\alpha}\text{FA}_\alpha\text{PbI}_{3-\beta}\text{X}_\beta$  ( $\text{X} = \text{Cl}, \text{Br}$ ) explored for photovoltaic applications. *RSC Adv.* **2019**, *9*, 7015–7024. [CrossRef]
7. Park, N.-G. Green solvent for perovskite solar cell production. *Nat. Sustain.* **2020**, *4*, 192–193. [CrossRef]
8. Vidal, R.; Alberola-Borràs, J.-A.; Habisreutinger, S.N.; Gimeno-Molina, J.-L.; Moore, D.T.; Schloemer, T.H.; Mora-Seró, I.; Berry, J.J.; Luther, J.M. Assessing health and environmental impacts of solvents for producing perovskite solar cells. *Nat. Sustain.* **2020**, *4*, 277–285. [CrossRef]
9. Chang, J.; Wang, G.; Huang, Y.; Luo, X.; Chen, H. New insights into the electronic structures and optical properties in the orthorhombic perovskite  $\text{MAPbI}_3$ : A mixture of Pb and Ge/Sn. *New J. Chem.* **2017**, *41*, 11413–11421. [CrossRef]
10. Im, J.H.; Jang, I.H.; Pellet, N.; Grätzel, M.; Park, N.G. Growth of  $\text{CH}_3\text{NH}_3\text{PbI}_3$  cuboids with controlled size for high-efficiency perovskite solar cells. *Nat. Nanotechnol.* **2014**, *9*, 927–932. [CrossRef]
11. Cao, X.; Hao, L.; Liu, Z.; Su, G.; He, X.; Zeng, Q.; Wei, J. All green solvent engineering of organic-inorganic hybrid perovskite layer for high-performance solar cells. *Chem. Eng. J.* **2022**, *437*, 135458. [CrossRef]

12. Hamill, J.J.C.; Schwartz, J.; Loo, Y.-L. Influence of Solvent Coordination on Hybrid Organic–Inorganic Perovskite Formation. *ACS Energy Lett.* **2017**, *3*, 92–97. [[CrossRef](#)]
13. Cai, B.; Zhang, W.-H.; Qiu, J. Solvent engineering of spin-coating solutions for planar-structured high-efficiency PSCs. *Chin. J. Catal.* **2015**, *36*, 1183–1190. [[CrossRef](#)]
14. Zhang, P.; Gu, N.; Song, L.; Chen, X.; Du, P.; Zha, L.; Chen, W.-H.; Xiong, J. The disappearing additive: Introducing volatile ethyl acetate into a perovskite precursor for fabricating high efficiency stable devices in open air. *Nanoscale* **2022**, *14*, 5204–5213. [[CrossRef](#)]
15. Doolin, A.J.; Charles, R.G.; De Castro, C.S.P.; Rodriguez, R.G.; Péan, E.V.; Patidar, R.; Dunlop, T.; Charbonneau, C.; Watson, T.; Davies, M.L. A universal co-solvent dilution strategy enables facile and cost-effective fabrication of perovskite photovoltaics. *Nat. Commun.* **2022**, *13*, 89. [[CrossRef](#)]
16. Cao, X.; Zhi, L.; Jia, Y.; Li, Y.; Zhao, K.; Cui, X.; Ci, L.; Zhuang, D.; Wei, J. A Review of the Role of Solvents in Formation of High-Quality Solution-Processed Perovskite Films. *ACS Appl. Mater. Interfaces* **2019**, *11*, 7639–7654. [[CrossRef](#)]
17. Rahimnejad, S.; Kovalenko, A.; Forés, S.M.; Aranda, C.; Guerrero, A. Coordination Chemistry Dictates the Structural Defects in Lead Halide Perovskites. *ChemPhysChem* **2016**, *17*, 2795–2798. [[CrossRef](#)]
18. Saidaminov, M.I.; Abdelhady, A.L.; Maculan, G.; Bakr, O.M. Retrograde solubility of formamidinium and methylammonium lead halide perovskites enabling rapid single crystal growth. *Chem. Commun.* **2015**, *51*, 17658–17661. [[CrossRef](#)] [[PubMed](#)]
19. Khlyabich, P.P.; Loo, Y.-L. Crystalline Intermediates and Their Transformation Kinetics during the Formation of Methylammonium Lead Halide Perovskite Thin Films. *Chem. Mater.* **2016**, *28*, 9041–9048. [[CrossRef](#)]
20. Stewart, R.J.; Grieco, C.; Larsen, A.V.; Doucette, G.S.; Asbury, J.B. Molecular Origins of Defects in Organohalide Perovskites and Their Influence on Charge Carrier Dynamics. *J. Phys. Chem. C* **2016**, *120*, 12392–12402. [[CrossRef](#)]
21. Xu, Y.; Wang, M.; Lei, Y.; Ci, Z.; Jin, Z. Crystallization Kinetics in 2D Perovskite Solar Cells. *Adv. Energy Mater.* **2020**, *10*, 2002558. [[CrossRef](#)]
22. Gao, L.; Zhang, F.; Xiao, C.; Chen, X.; Larson, B.W.; Berry, J.J.; Zhu, K. Improving Charge Transport via Intermediate-Controlled Crystal Growth in 2D Perovskite Solar Cells. *Adv. Funct. Mater.* **2019**, *29*, 1901652. [[CrossRef](#)]
23. Konstantakou, M.; Perganti, D.; Falaras, P.; Stergiopoulos, T. Anti-Solvent Crystallization Strategies for Highly Efficient Perovskite Solar Cells. *Crystals* **2017**, *7*, 291. [[CrossRef](#)]
24. Nemnes, G.A.; Besleaga, C.; Tomulescu, A.G.; Palici, A.; Pintilie, L.; Manolescu, A.; Pintilie, I. How measurement protocols influence the dynamic J-V characteristics of perovskite solar cells: Theory and experiment. *Sol. Energy* **2018**, *173*, 976–983. [[CrossRef](#)]
25. Tomulescu, A.G.; Stancu, V.; Beşleagă, C.; Enculescu, M.; Nemnes, G.A.; Florea, M.; Dumitru, V.; Pintilie, L.; Pintilie, I.; Leonat, L. Reticulated Mesoporous TiO<sub>2</sub> Scaffold, Fabricated by Spray Coating, for Large-Area Perovskite Solar Cells. *Energy Technol.* **2019**, *8*, 1900922. [[CrossRef](#)]
26. Liu, J.; Li, N.; Jia, J.; Dong, J.; Qiu, Z.; Iqbal, S.; Cao, B. Perovskite films grown with green mixed anti-solvent for highly efficient solar cells with enhanced stability. *Sol. Energy* **2019**, *181*, 285–292. [[CrossRef](#)]
27. Taylor, A.D.; Sun, Q.; Goetz, K.P.; An, Q.; Schramm, T.; Hofstetter, Y.; Litterst, M.; Paulus, F.; Vaynzof, Y. A general approach to high-efficiency perovskite solar cells by any antisolvent. *Nat. Commun.* **2021**, *12*, 1878. [[CrossRef](#)]
28. Scherrer, P. Bestimmung der Größe und der inneren Struktur von Kolloidteilchen mittels Röntgenstrahlen. *Nachr. Ges. Wiss. Göttingen. Math. Phys. Kl.* **1918**, *1918*, 98–100.
29. Zaman, M.M.U.; Imran, M.; Saleem, A.; Kamboh, A.H.; Arshad, M.; Khan, N.A.; Akhter, P. Potassium doped methylammonium lead iodide (MAPbI<sub>3</sub>) thin films as a potential absorber for perovskite solar cells; structural, morphological, electronic and optoelectric properties. *Phys. B Condens. Matter* **2017**, *522*, 57–65. [[CrossRef](#)]
30. Shen, W.Z. A Novel Approach for the Evaluation of Band Gap Energy in Semiconductors. *Int. J. Infrared Millim. Waves* **2002**, *23*, 61–69. [[CrossRef](#)]
31. Derbali, S.; Nouneh, K.; Florea, M.; Leonat, L.; Stancu, V.; Tomulescu, A.; Galca, A.; Secu, M.; Pintilie, L.; Touhami, M.E. Potassium-containing triple-cation mixed-halide perovskite materials: Toward efficient and stable solar cells. *J. Alloys Compd.* **2020**, *858*, 158335. [[CrossRef](#)]
32. Chueh, C.-C.; Li, C.-Z.; Jen, A.K.-Y. Recent Progress and Perspective in Solution-Processed Interfacial Materials for Efficient and Stable Polymer and Organometal Perovskite Solar Cells. *Energy Environ. Sci.* **2015**, *8*, 1160–1189. [[CrossRef](#)]
33. Mehdi, H.; Leonat, L.N.; Stancu, V.; Saidi, H.; Enculescu, M.; Tomulescu, A.G.; Toma, V.; Pintilie, I.; Bouazizi, A.; Galca, A.C. Effect of chlorine and bromine on the perovskite crystal growth in mesoscopic heterojunction photovoltaic device. *Mater. Sci. Semicond. Process.* **2022**, *143*, 106558. [[CrossRef](#)]
34. Stancu, V.; Leonat, L.N.; Tomulescu, A.G.; Derbali, S.; Pintilie, L.; Besleaga, C.; Galca, A.-C.; Neatu, F.; Neatu, S.; Florea, M.; et al. Influence of doping the inorganic cation with Eu or Sb on the properties of perovskite films. *Phys. Scr.* **2020**, *95*, 075707. [[CrossRef](#)]
35. Márquez, J.A.; Rusu, M.; Hempel, H.; Ahmet, I.Y.; Kölbach, M.; Simsek, I.; Choubrac, L.; Gurieva, G.; Gunder, R.; Schorr, S.; et al. BaZrS<sub>3</sub> Chalcogenide Perovskite Thin Films by H<sub>2</sub>S Sulfurization of Oxide Precursors. *J. Phys. Chem. Lett.* **2021**, *12*, 2148–2153. [[CrossRef](#)] [[PubMed](#)]
36. Richardson, G.; O’Kane, S.E.J.; Niemann, R.G.; Peltola, T.A.; Foster, J.M.; Cameron, P.J.; Walker, A.B. Can slow-moving ions explain hysteresis in the current–voltage curves of perovskite solar cells? *Energy Environ. Sci.* **2016**, *9*, 1476–1485. [[CrossRef](#)]

37. Nemnes, G.; Besleaga, C.; Tomulescu, A.; Pintilie, I.; Pintilie, L.; Torfason, K.; Manolescu, A. Dynamic electrical behavior of halide perovskite based solar cells. *Sol. Energy Mater. Sol. Cells* **2017**, *159*, 197–203. [[CrossRef](#)]
38. Filipoiu, N.; Preda, A.T.; Anghel, D.-V.; Patru, R.; Brophy, R.E.; Kateb, M.; Besleaga, C.; Tomulescu, A.G.; Pintilie, I.; Manolescu, A.; et al. Capacitive and Inductive Effects in Perovskite Solar Cells: The Different Roles of Ionic Current and Ionic Charge Accumulation. *Phys. Rev. Appl.* **2022**, *18*, 064087. [[CrossRef](#)]
39. Liu, P.; Wang, W.; Liu, S.; Yang, H.; Shao, Z. Fundamental Understanding of Photocurrent Hysteresis in Perovskite Solar Cells. *Adv. Energy Mater.* **2019**, *9*, 180301713. [[CrossRef](#)]
40. Anghel, D.-V.; Nemnes, G.A.; Pintilie, I.; Manolescu, A. Modelling  $J$ - $V$  hysteresis in perovskite solar cells induced by voltage poling. *Phys. Scr.* **2019**, *94*, 125809. [[CrossRef](#)]
41. Nemnes, G.A.; Besleaga, C.; Tomulescu, A.G.; Leonat, L.N.; Stancu, V.; Florea, M.; Manolescu, A.; Pintilie, I. The hysteresis-free behavior of perovskite solar cells from the perspective of the measurement conditions. *J. Mater. Chem. C* **2019**, *7*, 5267–5274. [[CrossRef](#)]
42. Zhang, W.; Li, Y.; Liu, X.; Tang, D.; Yuan, X. Ethyl acetate green antisolvent process for high-performance planar low-temperature SnO<sub>2</sub>-based perovskite solar cells made in ambient air. *Chem. Eng. J.* **2019**, *379*, 122298. [[CrossRef](#)]
43. Park, N.-G.; Zhu, K. Scalable fabrication and coating methods for perovskite solar cells and solar modules. *Nat. Rev. Mater.* **2020**, *5*, 333–350. [[CrossRef](#)]
44. Zhu, L.; Zhang, X.; Li, M.; Shang, X.; Lei, K.; Zhang, B.; Chen, C.; Zheng, S.; Song, H.; Chen, J. Trap State Passivation by Rational Ligand Molecule Engineering toward Efficient and Stable Perovskite Solar Cells Exceeding 23% Efficiency. *Adv. Energy Mater.* **2021**, *11*, 2100529. [[CrossRef](#)]

**Disclaimer/Publisher's Note:** The statements, opinions and data contained in all publications are solely those of the individual author(s) and contributor(s) and not of MDPI and/or the editor(s). MDPI and/or the editor(s) disclaim responsibility for any injury to people or property resulting from any ideas, methods, instructions or products referred to in the content.